# Selectivity and competition between the anodic evolution of oxygen and chlorine

Vos, J.G.

## Citation

Vos, J. G. (2019, December 4). *Selectivity and competition between the anodic evolution of oxygen and chlorine*. Retrieved from https://hdl.handle.net/1887/81383

**Author**: Vos, J.G.
**Title**: Selectivity and competition between the anodic evolution of oxygen and chlorine
**Issue Date**: 2019-12-04

# 6

# $MnO_x/IrO_x$ AS SELECTIVE OXYGEN EVOLUTION ELECTROCATALYST IN ACIDIC CHLORIDE SOLUTION

An OER-selective anode is highly desired, as this would allow the electrolysis of readily available seawater without the formation of (mainly) chlorine as toxic by-product. Unfortunately, previous literature and Chapter 3 of this thesis suggest strong scaling behavior between the OER and CER, as well as an intrinsic kinetic advantage of the CER over the OER, so that optimizing the efficiency of the OER over the CER in acidic media has proven especially difficult. In this regard, we have investigated the OER vs. CER selectivity of manganese oxide ($MnO_x$), a known OER catalyst with unusually high OER selectivity. Thin films (~5-20 nm) of $MnO_x$ were electrodeposited on glassy carbon-supported hydrous iridium oxide ($IrO_x$/GC), and tested for selectivity using rotating ring-disk electrode voltammetry and online electrochemical mass spectrometry. It was found that deposition of $MnO_x$ onto $IrO_x$ decreases the CER selectivity of the system in presence of 30 mM $Cl^-$ from 86% to less than 7%, making it a highly OER-selective catalyst. Detailed studies of the CER mechanism and ex-situ structure studies using SEM, TEM and XPS suggest that the $MnO_x$ film is in fact not a catalytically active phase, but functions as a permeable overlayer that disfavors the transport of chloride ions.

THIS CHAPTER IS BASED ON THE FOLLOWING

PUBLICATION:

Vos, J. G.; Wezendonk, T. A.; Jeremiasse, A. W.; Koper, M. T. M. MnOx/IrOx as Selective Oxygen Evolution Electrocatalyst in Acidic Chloride Solution. J. Am. Chem. Soc. 2018, 140 (32), 10270–10281.

## 6.1. Introduction

An OER-selective anode would allow the direct splitting of saline water without the costly need of removing chloride from the system. Unfortunately, anodes that are highly OER selective in presence of $\mathrm{Cl}^-$ are very rare, due to the favorable kinetics of the CER and the scaling between OER vs. CER activities described previously. A notable exception is manganese oxide ($\mathrm{MnO_x}$), an OER-active material that has received significant interest in recent years.[233–236] Initially reported by Bennet,[25] anodes based on $\mathrm{MnO_x}$ show a strong tendency to selectively evolve oxygen from acidic saline water. Hashimoto *et al.* studied a series of Mn-based mixed metal oxides (MMO) deposited on an $\mathrm{IrO_x/Ti}$ substrate and showed that such anodes often exhibit nearly 100% selectivity towards OER, under a variety of experimental conditions, for many hours of sustained operation.[31,237–239] Besides its high reported OER selectivity, $\mathrm{MnO_x}$ is also one of the few non-precious metal-based catalysts that has been reported to be moderately stable in acid under OER conditions.[240] This stability is in strong contrast with other 3d metal oxides such as $\mathrm{CoO_x}$ and Ni/Fe based oxyhydroxides, materials which show very high OER activity in alkaline pH, but are unstable and inactive in acid.[66,177,241–245]

In this chapter, we investigate the origin of the exceptional OER selectivity of the $\mathrm{MnO_x}$-based materials studied by Hashimoto and co-workers. To our knowledge, the mechanism by which $\mathrm{MnO_x}$ 'breaks the scaling' between the OER and CER was never thoroughly investigated. In part, we believe this was due to the difficulty of reliably measuring OER vs. CER activity *in situ*, for which no fast, practical method existed. Fortunately, the RRDE method described in Chapter 2 can be conveniently employed for rapid and precise CER activity measurement in this particular system. We will use the RRDE method to study the effect of $\mathrm{MnO_x}$ deposition onto $\mathrm{IrO_x}$ with respect to the OER and CER selectivity during cycling voltammetry and amperometry. Product species are also studied using online electrochemical mass spectrometry (OLEMS) measurements in combination with isotopic labelling. To gain more insight in the nature of the $\mathrm{MnO_x}$ film, *ex situ* studies of the catalyst were performed using bulk X-ray diffraction (XRD), scanning electron microscopy (SEM), transmission electron microscopy (TEM), and X-ray photoelectron microscopy (XPS). In this way, we aim to shed more light on the mechanism by which $\mathrm{MnO_x}$-based anodes selectively evolve oxygen, and how selectivity between the OER and CER may be better controlled.

## 6.2. Experimental

### 6.2.1. Chemicals

$\mathrm{KHSO_4}$, $\mathrm{HClO_4}$ (60%), KCl, NaCl, KBr and $\mathrm{NaClO_4}$ (EMSURE) were purchased from Merck. $\mathrm{Na_2IrCl_6 \cdot 6H_2O}$ (99.9%, trace metals basis) and NaOH (30% solution, TraceSelect) were purchased from Sigma-Aldrich. $\mathrm{MnSO_4}$ (99.999%) and $\mathrm{Mn(ClO_4)_2}$ (99.995%) were purchased from Alfa Aesar. High purity isotopically labeled water (97% $^{18}$O, >99.99%) was purchased from Cortecnet. All chemicals were used as received. The water used for all experiments except those involving isotopic labelling was prepared by a Merck Millipore Milli-Q system (resistivity 18.2 MΩcm, TOC < 5 p.p.b.).

### *6.2.2. General electrochemical procedures*

All experiments were carried out at room temperature (~20 °C). The electrochemical experiments were done using home-made two-compartment borosilicate glass cells with solution volumes of 100 mL. $IrO_x$ deposition experiments and sample preparation for structural studies were done in borosilicate glass vials of approximately 10 mL. Before the first-time use, all glassware was thoroughly cleaned by boiling in a 3:1 mixture of concentrated $H_2SO_4$ and $HNO_3$. When not in use, all glassware was stored in a 0.5 M $H_2SO_4$ solution containing 1 g/L $KMnO_4$. Before each experiment, glassware was thoroughly rinsed with water, and then submerged in a dilute (~0.01 M) solution of $H_2SO_4$ and $H_2O_2$ to remove all traces of $KMnO_4$ and $MnO_2$. The glassware was then rinsed three times with water and boiled in water. The rinsing-boiling procedure was repeated two more times. An IviumStat potentiostat (Ivium Technologies) was used during electrochemistry experiments. All experiments except $IrO_x$ deposition experiments and sample preparations for structural studies were 85% iR-compensated. The solution resistance was measured with electrochemical impedance spectroscopy, by observing the absolute impedance in the high frequency domain (100-10 KHz) corresponding to a zero-degree phase angle. RRDE and OLEMS experiments were performed in 0.5 M $KHSO_4$ solutions with pH values in the range of 0.88 ± 0.05, as measured with a Lab 855 meter equipped with a glass electrode (SI Analytics). Working solutions used in RRDE and OLEMS experiments were saturated with Ar (Linde, purity 6.0) before experiments. Solutions were bubbled with Ar gas during forced convection experiments, and Ar was used to blanket the solution in case of OLEMS. The reference electrode for RRDE and OLEMS experiments was a HydroFlex® reversible hydrogen electrode (Gaskatel), separated from the main solution using a Luggin capillary, to fix the reference sensing point and to prevent mixed potentials at the reference due to dissolved $Cl_2$ gas. A LowProfile Ag/AgCl electrode (Pine Research Instrumentation, sat. KCl, E = 0.197 V vs. NHE) was used during $IrO_x$ deposition experiments and sample preparations for structural studies. All potentials in this chapter are reported using the RHE scale unless specified otherwise. The Ag/AgCl reference was regularly calibrated versus the RHE to check its equilibrium potential. A Pt mesh was used as counter electrode during RRDE and OLEMS experiments. During $IrO_x$ deposition experiments and sample preparations for structural studies, the counter electrode was a Pt spiral placed axisymmetrically below the RRDE tip.

### *6.2.3. Rotating ring-disk studies (RRDE) of chlorine evolution vs. $MnO_x$ deposition*

RRDE measurements were done with an MSR rotator and E6 ChangeDisk RRDE tips in a PEEK shroud (Pine Research). The Luggin tip connected to the reference electrode was aligned to the center of the RRDE electrode to minimize electrical cross-talk.[137,138] The liquid phase collection factor of the ring-disk system, $N_l$, was determined by studying the $Fe[CN]_6^{3-}/Fe[CN]_6^{4-}$ redox couple in a solution of 10 mM $K_3Fe[CN]_6$ and 0.1 M $KNO_3$, using the Pt ring with both a freshly prepared blank GC electrode and the $IrO_x$/GC electrode. The value was 0.244 within 5% accuracy. The collection factor for dissolved $Cl_2$ was also measured in the same setup, by evolving chlorine selectively on a Pt disk electrode at 1.6 V vs. RHE, well before the kinetic onset of OER. Provided that the solution pH was lower than 1, the collection factor for dissolved chlorine was found to be 0.240, almost identical to $N_l$.

$IrO_x$/GC electrodes were prepared via electroflocculation of $IrO_x$ nanoparticles, as described in sections 9.1.1 and 9.1.2. The GC surfaces were polished with diamond paste, followed by rinsing and sonication in water for 3 minutes. The electroflocculation amperometry step lasted 300 s.

Before RRDE experiments, the Pt ring was electropolished by scanning from –0.1 V to 1.7 V at 500 mV $s^{-1}$ for 40 scans at 1500 RPM, after which the individual scans did not change. This step was vital to remove traces of $IrO_x$ that deposited on the ring during $IrO_x$ electroflocculation under rotation.[139] Hydrodynamic experiments were done at 1500 RPM by scanning the disk electrode in the range of 1.1 – 1.55 V at 10 mV $s^{-1}$. The ring was kept at 0.95 V during measurement of CER rates. Presence of $Mn^{2+}$ is not expected to interfere with the Pt ring during experiments.[177,246] In between experiments, the $IrO_x$/GC electrode was kept at 1.1 V. Ring currents were corrected for constant background currents and product collection delay. The latter arises from the time needed for products formed on the disk to reach the ring, and was approximately 200 ms at 1500 RPM. Before initiating quantitative measurements, the $IrO_x$/GC electrode was scanned 40 times in a chloride-free electrolyte between 1.3 – 1.55 V (into the OER region) at 1500 RPM. This was done to ensure stable $IrO_x$ film behavior during experiments. All currents were reported without normalization to catalyst surface area, since we were solely interested in selectivity trends (which are ratios of currents) and kinetic parameters such as Tafel slopes, none of which are affected by normalization.

### 6.2.4. Online electrochemical mass spectroscopy (OLEMS)

During OLEMS experiments, volatile reaction products were collected *in situ* using a 0.5 mm diameter tip with a porous PTFE membrane at a close distance (~10 μm) to the electrode surface, positioned with a micrometric screw system.[247] Mass signals were measured using an EvoLution mass spectrometer setup (ESS Ltd.) equipped with a Balzers QMS200 quadrupole (Pfeiffer). Pressure in the mass chamber was maintained lower than $10^{-6}$ mbar using a rotary vane pump (Edwards nXDS6i) and a TMH-071P turbo molecular pump (Pfeiffer). Before experiments, the tip was cleaned by submerging it for 1 hour in a mixture of 0.2 M $K_2Cr_2O_7$ and 2 M $H_2SO_4$, followed by ample rinsing with water. The $IrO_x$/GC disk working electrode was prepared as described in section 9.1.2, after which the disk was carefully removed from the RRDE tip and mounted to a stiff Pt wire using Cu tape. The electrode was then mounted in hanging-meniscus configuration. The Luggin tip connected to the RHE reference was placed sideways near the working electrode at a distance of approximately 1.5 cm, to accommodate the OLEMS tip. Isotopic labelling was performed in a 1.5 mL volume of 0.1 M $KHSO_4$ in $H_2{}^{18}O$, using a LowProfile Ag/AgCl reference and a Pt spiral as counter electrode. The reference electrode was temporarily stored in a 0.1 M $KHSO_4$ solution of regular water in-between experiments, to minimize $Cl^-$ leakage into the isotopic solution. The $IrO_x$ electrode surface was first rinsed with $H_2{}^{16}O$ water and thoroughly dried using filtered compressed air. Ir $^{18}O$-exchange was done by performing OER at 1.25 V vs. Ag/AgCl for 300 s, followed by thorough rinsing with $H_2{}^{16}O$ water. The '$Ir^{18}O_x$'/GC electrode was submerged in the OLEMS cell strictly under potential control at 1.30 V, followed by $MnO_x$ deposition and scanning experiments.

### *6.2.5. Sample deposition for structural studies*

$IrO_x$/GC samples were prepared via deposition of $IrO_x$ onto a GC disk, as described in section 9.1.2. $MnO_x$ films were grown in solutions of 0.35 M $NaClO_4$ + 0.15 M $HClO_4$ (pH = 0.88) in presence of 0.6 mM $Mn(ClO_4)_2$. The use of a non-adsorbing $ClO_4^-$ electrolyte allowed $MnO_x$ deposition at lower potentials, in absence of superimposed OER (in case $IrO_x$ was the substrate), leading to more accurate monitoring of film growth. This was necessary as it was not possible to verify the film thickness post-analysis from reductive dissolution. $MnO_x/IrO_x$/GC and $MnO_x$/GC samples were prepared by conditioning an $IrO_x$/GC or blank GC disk electrode at 1.45 V and 1500 RPM. In case $IrO_x$ was the substrate, 20 mM NaCl was added to the solution and $MnO_x$ film formation on $IrO_x$ was monitored by keeping the ring electrode at 0.95 V and measuring the CER rate. For preparation of a $MnO_x$/GC sample, deposition of the film was stopped near ~1.25 * $t_{max}$, $t_{max}$ being the time corresponding to the peak current during deposition.[248] In all cases, when a satisfactory $MnO_x$ coverage was reached, the experiment was discontinued by raising the working electrode while rotating, breaking electrical contact and spin-drying the surface. This procedure was employed to minimize transient $MnO_x$ dissolution in the acidic environment. Immediately after spin-drying, the electrode was rinsed with ample water and dried with compressed filtered air.

### *6.2.6. Scanning electron microscopy (SEM)*

GC disks were carefully removed from the RRDE tip after deposition and glued to a SEM specimen mount using conductive silver epoxy. Scanning electron micrographs were made using a FEI Nova NanoSEM 200 equipped with a field emission electron source, operating at 10 kV beam accelerating voltage and 10 pA probe current. Images were recorded in immersion mode using a through-the-lens detector, at a working distance of ~4.5 mm. EDS measurements were performed in a JSM 6010LA setup (JEOL). After recording overview images at 10 kV, the beam accelerating voltage was increased to 15 kV and elemental data were recorded from a wide variety of locations on the electrode.

### *6.2.7. Transmission electron microscopy (TEM)*

GC disks were carefully removed from the RRDE tip after deposition, and the $IrO_x/MnO_x$ films were then carefully scraped off the electrode surface. The films were sonicated for 30 minutes in absolute ethanol, and the suspension was dropcasted onto a Cu TEM grid. Bright-field transmission micrographs were recorded using a JEM-1400Plus apparatus (JEOL) equipped with a $LaB_6$ filament and a 2kx2k Orius camera (Gatan), operating at 120 kV accelerating voltage. For measurements at higher resolution, a model JEM-2010 (JEOL) equipped with a $LaB_6$ filament and an Orius 831 camera (Gatan) was used, operating at 200 kV. Selected-area diffraction patterns were analyzed using the CrysTBox software suite.[249]

### 6.2.8. X-ray diffraction measurements (XRD)

GC disks were carefully removed from the RRDE tip after deposition and mounted directly in the diffractometer using a height-adjustable mount to correct for disk protrusion. X-ray diffraction spectra were recorded using a D8-Advance diffractometer (Bruker) operated in Bragg-Brentano geometry, equipped with a Co-Kα anode (λ = 1.78897 Å) and a Lynxeye position sensitive detector. Diffraction data were collected over angles ranging between 10° - 100° with a step size of 0.02° and scan speed of 0.2° $s^{-1}$.

### 6.2.9. X-ray photoelectron spectroscopy (XPS)

GC disks were carefully removed from the RRDE tip after deposition and mounted directly in the spectrometer. X-ray photoelectron spectroscopy measurements were performed in a K-alpha spectrometer (Thermo Fisher Scientific) using a monochromatic Al-Kα X-ray source. The measurements were carried out at a chamber pressure of about $10^{-8}$ mbar, a flood gun was used for charge compensation. The energy analyzer was operated with a pass energy of 200 eV and 0.25 eV energy spacing for the survey spectrum, and a pass energy of 50 eV and 0.1 eV energy spacing for the high-resolution spectrum. All binding energies were referenced to the C1s peak (284.8 ± 0.025 eV). Each spectrum reported is the statistical average of 10 measured scans. Spectral peaks were analyzed and processed using Thermo Avantage v5.903 software (Thermo Fisher Scientific). The Shirley algorithm was used to calculate background contributions. Relative atomic contributions on the surface were calculated using full width integration over the core-level signals along with tabulated atomic sensitivity factors (ASF). For the core-level Ir 4f peak deconvolution, we used a model from existing literature, excluding contributions from 4f satellite peaks.[250]

## 6.3. Results and discussion

### *6.3.1. Effect of $MnO_x$ deposition on chlorine evolution*

We make use of rotating ring-disk electrode voltammetry to measure and separate individual OER and CER currents, as described in Chapter 2. During these experiments, the collection factor for $Cl_2$ ($N_l$) was reproducible within 2%, and virtually identical to that of the $Fe[CN]_6^{2-}/Fe[CN]_6^{3-}$ redox couple ($N_l = 0.244$). Figure 6.1 illustrates a experiment of parallel OER and CER on $IrO_x$/GC, while scanning the disk potential in the range of 1.1 – 1.55 V in chloride concentrations of $[Cl^-] = 0$ mM and $[Cl^-] = 30$ mM (see also Figure 2.1). By observing the ring current in Figure 6.1, the onset of CER can be located at around 1.42 V, which means that it proceeds with negligible overpotential at pH = 0.88. Similar to results in Chapter 2, the OER is not strongly affected by either the presence of $Cl^-$ or parallel CER under the used conditions. Furthermore, selectivity towards CER is approximately 86% near 1.55 V. Although a chloride concentration of 30 mM is far removed from realistic seawater concentrations, which typically exceed 0.5 M, the use of such concentrations would compromise the ability to carry out fundamental CER studies, due to increasing experimental noise levels and interference of gas bubbles in the RRDE setup. In consideration of results from section 2.3.4, a concentration of 30 mM chloride should constitute an optimal system for study.

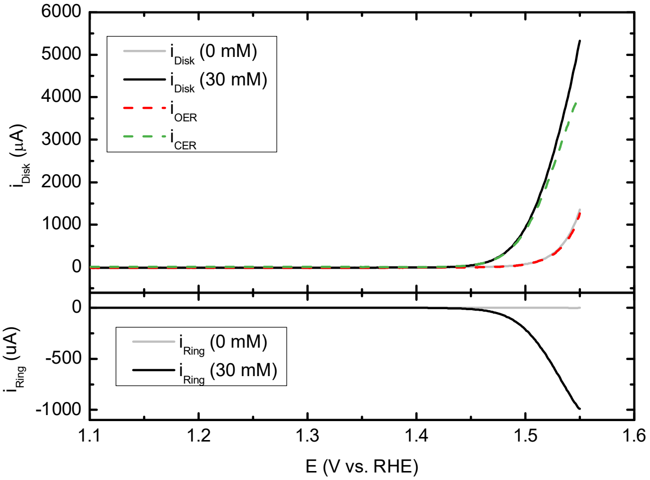

*Figure 6.1: Potential scans of mixed OER and CER in 0.5 M $KHSO_4$ (pH = 0.88), on a 'bare' $IrO_x$/GC electrode (no $MnO_x$). Top panel displays currents measured on the $IrO_x$/GC disk ($i_D$) in a $Cl^-$-free solution (grey curve), and in presence of 30 mM KCl (black curve). Rotation rate: 1500 RPM. Lower panel shows corresponding currents on the Pt ring ($i_R$) fixed at $E_R = 0.95$ V. Calculation of $i_{OER}$ and $i_{CER}$ curves was performed using Eq. 2.1 and Eq. 2.2.*

In acidic media, deposition of $MnO_x$ can proceed via the following overall reaction:

$$2\ Mn^{2+} + 2\ H_2O \rightarrow MnO_2 + 4\ H^+ + 2\ e^- \qquad \text{Eq. 6.1}$$

$$E^0_{MnO_x/Mn^{2+}} = (1.23 - 0.059 * \mathrm{pH})\ \mathrm{V\ vs.\ RHE}$$

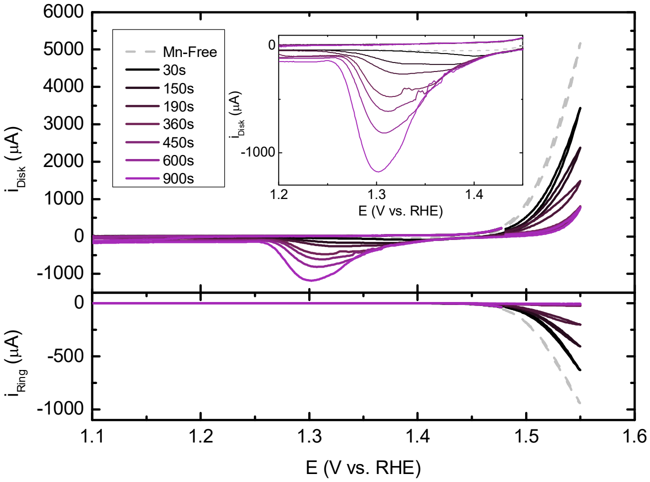

*Figure 6.2: Top panel shows CVs of an $IrO_x$/GC rotating disk electrode (top) in 0.5 M $KHSO_4$, 30 mM KCl (pH = 0.88), and 0.6 mM $MnSO_4$ (except for the $Mn^{2+}$-free experiment). Rotation rate: 1500 RPM. $MnO_x$ films were preconditioned at various times at 1.48 V before initiating the forward scan at 1.48 V. The lower panel shows the corresponding $i_R$ ($E_R = 0.95\ V$).*

To form $\mathrm{MnO_x}$ films on $\mathrm{IrO_x}$ and study their effect on CER selectivity, we resorted to growing $\mathrm{MnO_x}$ thin films *in situ* by 'spiking' the working solution with 0.6 mM $\mathrm{MnSO_4}$. This small but significant concentration of $\mathrm{Mn^{2+}}$ ions prevents the net dissolution of the acid-unstable $\mathrm{MnO_x}$ films during experiments.[240,251] Despite obvious disadvantages, such as lack of precise control over film thickness during scanning, this method allows the growth and study of thin $\mathrm{MnO_x}$ films of variable thickness in an identical system, without the severe uncertainty of the film's integrity (and problems concerning build-up of dissolved $\mathrm{Mn^{2+}}$ in the solution, in case of repeated externally grown $\mathrm{MnO_x}$ films). It is thus possible to measure how CER kinetics depend on $\mathrm{MnO_x}$ film growth. Figure 6.2 shows CVs from 1.1 – 1.55 V of an $\mathrm{IrO_x}$/GC electrode, in presence of 30 mM KCl and 0.6 mM $\mathrm{MnSO_4}$, under 1500 RPM rotation rate. Compared to a $\mathrm{Mn^{2+}}$-free solution, $\mathrm{MnO_x}$ deposition manifests itself as a superimposed current with a slow onset near 1.37 V (see Figure A 9.6.4 for a close-up). To grow $\mathrm{MnO_x}$ films of variable thickness and to test their effect on CER activity, the disk electrode was first conditioned at $E_D = 1.48$ V, while rotating at 1500 RPM. The conditioning potential was chosen such that it was more positive than $E^{eq}_{MnO_x/Mn^{2+}}$ (approximately 1.13 V at pH = 0.88), but not too far into the mixed OER/CER region in order to prevent excessive gas formation during deposition. Immediately after conditioning, the electrode was scanned up to a positive potential limit of $E_D = 1.55$ V. At the same time, the ring was kept at $E_R = 0.95$ V, and still regarded as a selective probe for chlorine. Formation of $\mathrm{Cl_2}$ can be seen in both the forward and reverse sweep. During the reverse scan, complete cathodic dissolution of the $\mathrm{MnO_x}$ films appears as a reduction wave from approximately 1.450 to 1.15 V. Dissolution of the film effectively 'resets' the working electrode, and the charge under the reduction peak (described as $Q_{MnO_x}$) allows to approximate the thickness of the film that was originally present in the forward scan. Repeated scanning without preconditioning led to overlapping CVs, with reproducible peak currents, ring currents and cathodic $MnO_x$ dissolution peaks, which shows that the original system is restored every time after traversing the negative potential limit of 1.10 V (see Figure A 9.6.5). A $Mn^{2+}$ concentration of 0.6 mM was purposefully tested as optimum: lower concentrations led to impractically long deposition times, and higher $[Mn^{2+}]$ (> 1 mM) often resulted in films that were too thick to completely dissolve after returning to 1.10 V. This was evident from a remaining brown-red glow on the electrode surface, and significant but slowly subsiding negative current when the potential was kept at 1.10 V. Thicker films also occasionally led to mechanical instability in the form of brown $MnO_x$ flakes peeling off the electrode during rotation. Keeping $[Mn^{2+}]$ as low as possible also reduced the extent of continuous (uncontrolled) $MnO_x$ deposition current during scanning and allowed a more accurate comparison of $i_{OER}$ and $i_{CER}$, as will be discussed below.

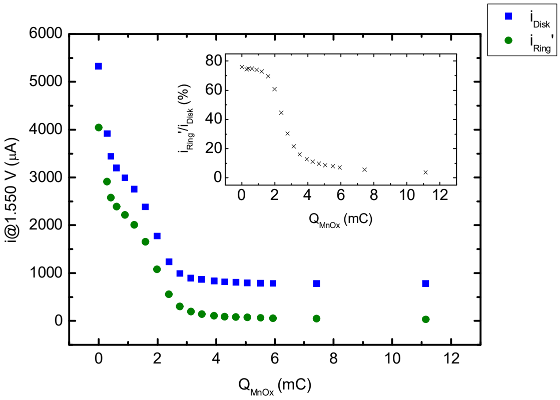

*Figure 6.3: Disk (blue) and ring currents (green) measured at $E_D = 1.55$ V as function of $Q_{MnO_x}$, the reductive charge measured for the corresponding $MnO_x$ film during the backward scan, which is an approximate measure of its thickness. Inset shows the ratio between $i_D$ and $i_R$ corrected for $N_l$ ($i_R$'). Values were determined from CVs such as those in Figure 6.2.*

Figure 6.3 displays the measured disk and ring currents for $E_D = 1.55$ V as a function of $Q_{MnO_x}$, the charge determined from the $MnO_x$ dissolution wave in the corresponding reverse sweeps. The potential of 1.55 V was chosen for quantitative analysis, since this is the point of potential reversal and as such contains minimal current contributions from (pseudo)capacitive processes. To be able to compare directly, ring currents $i_R$ are corrected for $N_l$ to obtain $i_R'$. The distinction between $i_R'$ and $i_{CER}$ will be discussed shortly. The deposition of $MnO_x$ has a profound effect on both $i_D$ and $i_R'$, but the most interesting aspect is the selectivity: $i_R'$ is impacted very differently than $i_D$. As $Q_{MnO_x}$ varies within 0 - 2 mC, a proportional decrease in both $i_D$ and $i_R'$ can be seen, leading to an approximately constant ratio $i_R'/i_D$ (Figure 6.3, inset). For $Q_{MnO_x}$ > 2 mC, the ratio $i_R'/i_D$ shows a sudden drop. We also observe a change in shape of the $MnO_x$ reduction wave as $Q_{MnO_x}$ increases above 2 mC. Below 2 mC, a single, broad reduction peak is observed, which transforms into two peaks for $Q_{MnO_x}$ > 2 mC, with peak potentials shifting continuously more negative as the reduction charge increases (see Figure A 9.6.6). The appearance of separate peaks may be due to proton diffusion becoming the limiting factor during film reductive dissolution.[252,253]

Unfortunately, the quantification of $i_{OER}$ and $i_{CER}$ in presence of $\mathrm{Mn^{2+}}$ is obfuscated by Mn-related redox processes, in contrast to the measurements on $\mathrm{MnO_x}$-free $\mathrm{IrO_x}$ in Figure 6.1, where it was assumed that the OER and CER were the sole reactions. There are two reasons for this. First, $i_D$ after subtraction of $i_R'$ is no longer 'pure' OER current, but the sum of OER and $\mathrm{MnO_x}$ deposition current. Second, close inspection of the ring currents (Figure A 9.6.4) suggests reduction of a species that appears at a potential slightly more negative than the onset potential of CER. We ascribe this additional current to the reduction of solution-phase $\mathrm{Mn^{3+}}$ .[254] This species is a generally accepted intermediate during acidic $\mathrm{MnO_x}$ deposition.[252,253,255] Ring currents can thus no longer be ascribed solely to CER ($i_R' \neq i_{CER}$). To take these two sources of error into account, we use the following correction. The diffusion limited current density of $\mathrm{MnO_x}$ deposition ($i^L_{MnO_x}$) is estimated at 140 μA using the Levich equation (see section 9.6.1). This value serves as an 'upper limit' of the $\mathrm{MnO_x}$ deposition current during the OER and CER. The maximum ring current originating from $\mathrm{Mn^{3+}}$ reduction can be estimated at 70 μA, representing an upper limit of ring current falsely attributed to CER. For $Q_{MnO_x} < 2$ mC, where $i_R' > 1800$ μA, this error was assumed negligible, but at $Q_{MnO_x} > 4$ mC, the remaining ring current approaches 30 μA. In this regime, the ring current may not be unambiguously assigned to CER, and the real CER current could be significantly lower.

To still make an estimation of OER vs. CER selectivity, we assume that i) $\mathrm{MnO_x}$ deposits with diffusion limited current densities at all potentials, allowing the calculation of the *minimum* OER current after ring current subtraction, and ii) $N_l$-corrected ring current $i_R'$ originates only from CER, irrespective of stray $\mathrm{Mn^{3+}}$ reduction reactions, leading to the *maximum possible* CER current. In other words, Eq. 2.1 applies, like the case for the 'blank' $\mathrm{IrO_x}$ catalyst: $i_R' = i_{CER}$. We thus use the following expression for $i_{OER}$:

$$i_{OER} = i_D - i_{CER} - i^L_{MnO_x} = i_D - i_R' - 140\ \mu\mathrm{A} \qquad \text{Eq. 6.2}$$

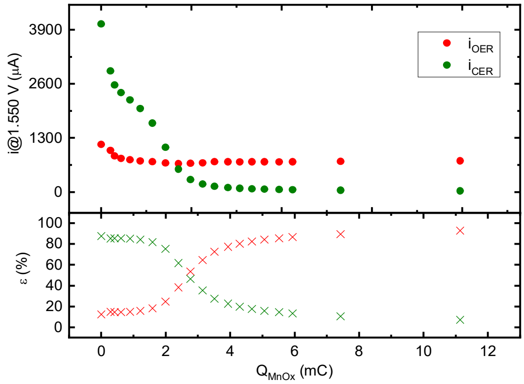

*Figure 6.4: Top panel: currents for OER (red) and CER (green) at $E_D = 1.55$ V (top), calculated from Eq. 2.1 and Eq. 6.2. Lower panel: corresponding selectivities towards OER (red) and CER (green). Data is plotted as a function of $Q_{MnO_x}$, the charge ascribed to the corresponding $MnO_x$ layer, which is an approximate indication of its thickness. Values were determined from CVs such as those in Figure 6.2.*

Figure 6.4 displays the calculated currents and selectivities towards the OER and CER as a function of $Q_{MnO_x}$. As already suggested by the ratio $i_R'/i_D$ in Figure 6.3, $\varepsilon_{OER}$ rises sharply at the expense of $\varepsilon_{CER}$ beyond a $MnO_x$ reduction charge of 2 mC. We will refer to the reduction charge of the $MnO_x$ film at which there is a strong shift of selectivity from CER towards OER as the 'critical $MnO_x$ charge'. Figure 6.4 shows that modification of $IrO_x$ by growth of a thick $MnO_x$ film makes it >90% OER selective with a moderate (45%) drop in activity.

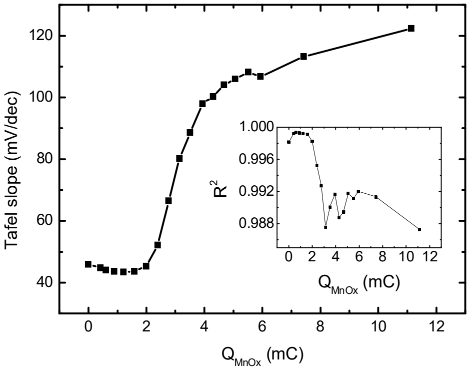

*Figure 6.5: Tafel slopes for CER on the disk electrode, constructed from ring currents, as a function of $Q_{MnO_x}$. Values taken from CVs similar to Figure 6.2. Inset shows corresponding $R^2$ values (correlation coefficients), to illustrate the degree of linearity as function of $Q_{MnO_x}$.*

The dependence of CER kinetics on $MnO_x$ deposition can be studied by making Tafel plots based on measured ring currents (Figure 6.5), especially at high ring currents where the error from $Mn^{3+}$ reduction is negligible. On 'bare' $IrO_x$, as well as during the initial stages of $MnO_x$ film growth ($Q_{MnO_x}$ < 2 mC), CER Tafel slopes range within 40-45 mV/dec, suggesting a rate-limiting second electron transfer step controlling the CER mechanism, in correspondence with previous literature.[56,105] The Tafel curves in this regime show good linearity, as determined from $R^2$-values in the inset of Figure 6.5. As $Q_{MnO_x}$ increases beyond the critical charge, Tafel slopes increase to ca. 120 mV/dec. This value agrees remarkably well with a mechanism where the first electron transfer step becomes rate-determining, suggesting that the apparent kinetics of the reaction change. However, a pronounced departure from linearity is also apparent (Figure 6.5, inset), suggesting that the measured Tafel slopes become clouded by additional effects. Above all, we expect the error from $Mn^{3+}$ reduction to be high here, and the measured Tafel slope may well be related to the solution phase oxidation of $Mn^{2+}_{aq}$ to $Mn^{3+}_{aq}$ on the disk (assuming a symmetry factor α of ~ ½).

To gain more insight in the sudden change in CER activity, ring-disk amperometry curves were recorded to study the potential-dependent deposition behavior of $MnO_x$ on $IrO_x$ (Figure 6.6). The ring currents in the lower panel were normalized versus their initial value ($i_{R,t=0}$), to compare the relative decrease in CER for different potentials. An increase in $E_D$ has a twofold effect: i) $i_D$ initially increases strongly, which is due to a rise in CER current (top panel), and ii) CER rates start declining earlier (lower panel). It was previously postulated that $MnO_x$ deposition proceeds through a progressive electrochemical nucleation and growth mechanism,

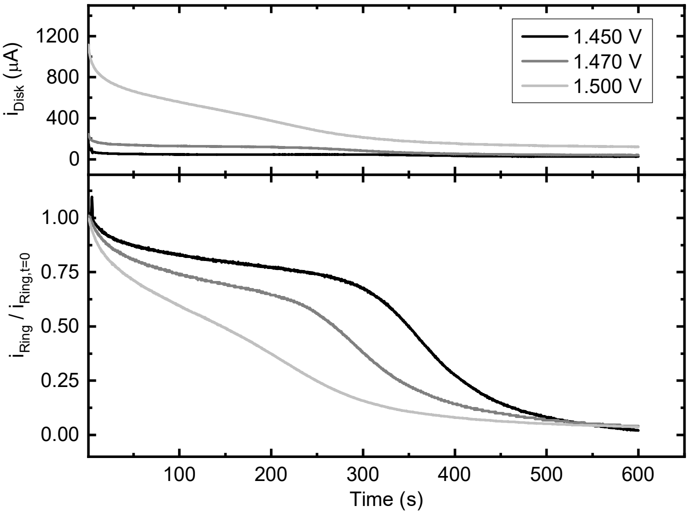

*Figure 6.6: Top panel: amperometry measurements at increasing potentials of an $IrO_x$/GC rotating disk electrode (top) in 0.5 M $KHSO_4$, 20 mM KCl, and 0.6 mM $MnSO_4$ (pH = 0.87), rotation rate 1500 RPM. The lower panel shows the corresponding $i_R$ normalized to their initial value $i_{R,t=0}$ ($E_R$ = 0.95 V).*

in which the current contribution from the growth of existing nuclei is larger than current from the formation of new nuclei.[248,256,257] The data presented here suggest that $MnO_x$ deposition at 1.45 V on amorphous $IrO_x$ near pH = 1 is kinetically controlled and proceeds via a similar mechanism, since the deposition current shows an induction time followed by a peak (Figure A 9.6.8). The observed drop in CER activity would then coincide with the moment where the exclusion zones of the individual $MnO_x$ nuclei intertwine and the full coverage of the $IrO_x$ surface by $MnO_x$ rapidly increases.

To corroborate the RRDE findings, we measured the competition of CER vs. OER on $IrO_x$ and the effect of $MnO_x$ deposition using OLEMS (Figure 6.7). Since the use of a stationary electrode is required in the OLEMS setup, a stirrer bar at ~600 rpm was used to enhance mass transport of chloride and $Mn^{2+}$, and reduce the effects of transient broadening of the diffusion layer. Despite this, mass transport to the surface was significantly lower than in the RRDE setup. To ensure a strong enough $Cl_2$ mass signal in the OLEMS and to reach $MnO_x$ film growth comparable to the RRDE experiments, a relatively high concentration of chloride (80 mM) and $MnSO_4$ (1.2 mM) was used. In Figure 6.7A, cyclic voltammetry was performed on an $IrO_x$/GC electrode with a significant amount of $MnO_x$ predeposited at 1.460 V, after which three cycles were carried out in the potential region of mixed CER, OER and $MnO_x$ deposition. The initial forward sweep starting from 1.460 V shows a relatively low maximum current, and the backward sweep shows a wave where the preformed $MnO_x$ layer is reductively removed. In scan 2 and 3, the $IrO_x$ electrode was scanned into the CER/OER region again, such that the electrode was free of pre-formed $MnO_x$. Mass signals m/z 32 and m/z 70 (corresponding to $O_2^+$ and $Cl_2^+$, ionized molecular oxygen and chlorine, respectively) were collected in the mass spectrometer during the scans. Both species have peaks in the mixed OER/CER region as expected, but there are major differences between the three cycles. The rate of $Cl_2$ formation

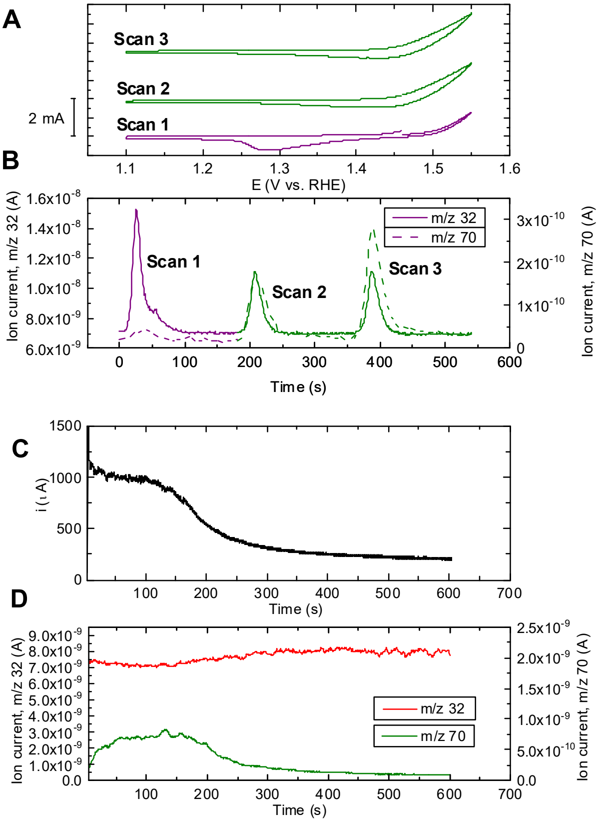

*Figure 6.7: OLEMS measurements of an $IrO_x$/GC disk electrode in 0.5 M $KHSO_4$, 80 mM KCl, and 1.2 mM $MnSO_4$ (pH = 0.89). A: CVs of the electrode after preconditioning for 450 s at 1.46 V, followed by three scans. Scan rate: 5 mV s$^{-1}$. C: Amperometry at 1.500 V for 600 s. Figures B and D show corresponding OLEMS mass signals over time. Solution saturated with Ar. A stirrer bar at ~600 rpm was employed to increase mass transport.*

is clearly suppressed during the first cycle, then strongly increases in cycle 2 and 3. The $O_2$ mass signal in the first scan shows significant trailing and is also higher than in scan 2 and 3. Comparison of results from scan 1 and scan 2 suggests that the emergence of CER activity is coupled to a decrease in OER activity. This appears to contradict the previous results from the RRDE method that the OER and CER are independent. However, we want to note that the amount of chlorine produced in cycle 2 and 3 was rather high, which was necessary to obtain a sizeable m/z 70 signal, as the majority of produced $Cl_2$ dissociates and recombines in the ionization chamber to form $HCl^+$, mass signal m/z 36.[77] It is thus highly likely that the collection efficiency of $O_2$ was affected by the vigorous chlorine evolution near the electrode surface. Nonetheless, we believe the most important result of the OLEMS measurements is the strong suppression of chlorine evolution in the first cycle, meaning that on an $IrO_x$/$MnO_x$ electrode, $O_2$ is formed highly selectively.

In Figure 6.7C, current vs. time curves were recorded at 1.50 V to investigate the effect of transient $MnO_x$ deposition, along with changes in $O_2$ and $Cl_2$ mass signals (Figure 6.7D). In the current profile, the semi-steady current declines abruptly after ~100 s, converging to a current of around 200 μA. The abrupt decline is reminiscent of results in Figure 6.6, and correlates with a selective decrease in the $Cl_2$ signal.

### 6.3.2. *Structure of the $MnO_x/IrO_x$ film*

The results in the previous sections show that during mixed OER and CER on an $IrO_x$ electrode covered by a $MnO_x$ film, there is a decrease in oxidation current coupled to strongly enhanced selectivity of OER over CER with an increase of the coverage by the $MnO_x$ film, as well as a change in the apparent CER Tafel slope. Besides the origin of this selectivity shift, a relevant question concerns the degree to which $MnO_x$ is catalytically active under these conditions. OLEMS measurements on a $MnO_x/GC$ sample in an acidic solution, without $IrO_x$ present, showed no detectable activity for OER or CER (Figure A 9.6.11), in accordance with previous literature. However, it has been reported that the crystal phase and oxide stoichiometry of $MnO_x$ as well as the existence of metal-support interactions, can greatly affect the OER performance.[258–261] Therefore, the structure of the deposited materials was studied.

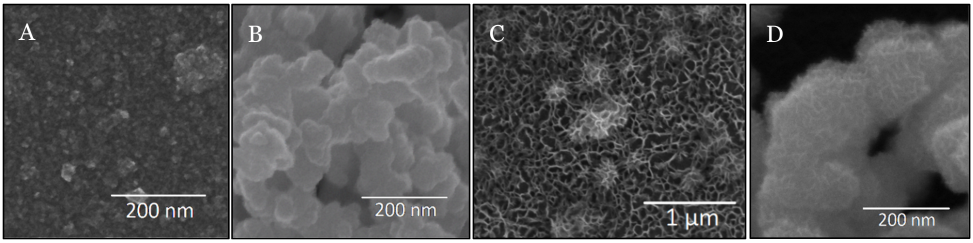

*Figure 6.8: SEM micrographs of representative electrodes used in this study. A and B: an $IrO_x/GC$ electrode, deposited according to the procedure described by Nakagawa et al. C and D: a $MnO_x/IrO_x/GC$ electrode, $MnO_x$ was deposited onto $IrO_x/GC$ as described in the text.*

For structural studies, films were grown hydrodynamically in $ClO_4^-$ solutions in presence of 20 mM $Cl^-$, allowing use of the ring electrode to monitor the rate of chlorine evolution during deposition. An amount of $MnO_x$ was deposited such that the CER rate was approximately 50% of the initial value (Figure A 9.6.9). The nature of the $MnO_x$ films in the following studies should therefore be close to films corresponding to the critical $MnO_x$ charge of 2 mC discussed earlier. $MnO_x$ films grown in $ClO_4^-$ and $HSO_4^-$ electrolytes showed identical morphologies in SEM and likewise behavior of $\varepsilon_{CER}$ vs. $Q_{MnO_x}$, suggesting that adsorption of $HSO_4^-$ inhibits $MnO_x$ deposition but does not alter its mechanism (Figure A 9.6.10).

Figure 6.8A shows a SEM micrograph of a representative $IrO_x/GC$ film, with a morphology corresponding well to previous reports.[142,143,262,263] The GC surface is covered by a thin layer of nanoparticulate $IrO_x$, as was revealed by drying-induced cracks of the film (see Figure A 9.6.15B). We also occasionally observed mesoporous clusters of $IrO_x$ particles with diameters of 50-150 nm (Figure 6.8B). The clusters generally occupied less than 4% of the GC electrode surface area, as estimated from SEM images of a large section of the electrode. Figure 6.8C and D show SEM micrographs of $MnO_x/IrO_x/GC$ samples, the films grown in the presence of 20 mM $Cl^-$ and representing '50% CER activity' compared to $MnO_x$-free conditions. A porous structure of thin intertwined sheets is visible on top of the $IrO_x$ particles and layer, which is composed of $MnO_x$, as verified via EDS analysis. From the SEM micrographs, the $MnO_x$ sheet thickness is within 8-10 nm (Figure A 9.6.15A). $MnO_x$ deposited on GC in absence of $IrO_x$ forms a similar structure (Figure A 9.6.15C). The $MnO_x$ morphologies resemble earlier SEM results of δ-$MnO_2$ (Birnessite), a poorly crystalline polymorph of $MnO_6$ octahedra arranged as sheets (see also Figure A 9.6.15D for a micrograph of $MnO_x$ formed during extended deposition times).[164,264–266] However, we cannot draw conclusions about the $MnO_x$ structure on the basis of SEM morphology alone.

We attempted to take XRD spectra of $IrO_x$ and the combined Mn/Ir oxide, using samples as-deposited on GC (see Figure A 9.6.14). Besides the GC background, no diffraction peaks were observed, suggesting that the $IrO_x$ and $MnO_x$ are amorphous. Previous studies of hydrated $IrO_x$ colloids, as well as $MnO_x$ deposited at constant potential, also reported amorphous structures.[248,258,263,267] It must be noted that the films may be too thin to lead to sufficient signal in the diffractometer, although an attempt was made to compare the diffraction patterns to a small quantity of highly crystalline $RuO_2$. Alternatively, $IrO_x$ nanoparticles were precipitated and isolated from acidified colloid solutions. Even when scanning such bulk samples, we could not observe XRD peaks.

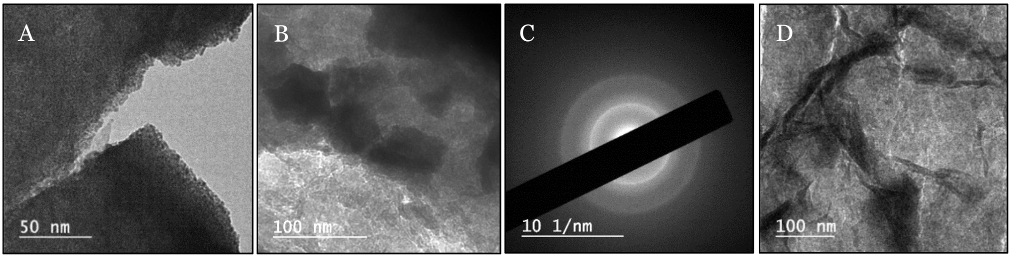

*Figure 6.9: TEM micrographs of a $MnO_x/IrO_x$ film that was grown identically to the films used for SEM in Figure 6.8, then carefully scraped off the GC support for imaging. A: Sheets of amorphous $IrO_x$ particles, having diameters in the range of 2-4 nm. B: Larger $IrO_x$ particles (diameter ~60 nm) within the film. C: SAED pattern of the area shown in B. Diffuse diffraction rings corresponding to rutile $IrO_2$ are visible. The also present $MnO_x$ does not generate a clear contribution to the pattern. D: Intertwined $MnO_x$ sheets perpendicular to the beam direction, as also seen in SEM micrographs.*

To obtain more structural information on the $MnO_x/IrO_x$ samples, TEM measurements were performed along with EDS and selected-area electron diffraction (SAED). Figure 6.9 shows bright-field TEM micrographs of a $MnO_x/IrO_x$ film that was carefully scraped off the GC electrode. $IrO_x$ nanoparticles with a diameter of 2-4 nm as well as occasionally larger particles were visible (Figure 6.9A and B), similar to results from Zhao *et al.*[262] Like the SEM results, a veiny $MnO_x$ deposit could be seen (verified by EDS), where the ~8 nm thick sheets were visible in the microscope (Figure 6.9D). Despite the much higher diffraction cross-section in comparison with XRD, most SAED experiments led to diffuse patterns. It was possible to sporadically obtain better defined radial profiles, roughly corresponding to rutile-$IrO_2$ (Figure 6.9C).[268,269] In the microscope, a rare instance of a crystallite that was also properly oriented showed a d-spacing of 3.18 Å, corresponding to the rutile $IrO_2$ (110) plane.[270] We also generated SAED patterns at higher beam accelerating voltages of 200 keV (Figure A 9.6.18), the result of which showed sporadic rutile-related diffractions from $IrO_2$ and β-$MnO_2$.

Unfortunately, significant contributions from metallic Ir (and possibly Mn) were also present, likely due to beam radiation damage.[170]

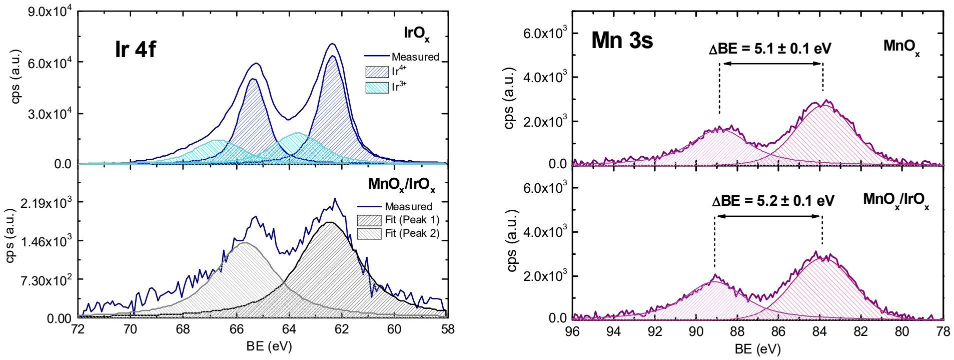

*Figure 6.10: Core-level XPS scans of the Ir 4f (left) and Mn 3s (right) spectral peaks, on an absolute intensity scale. Both elements were scanned in samples of their $MO_x$/GC single oxides (top panels) and the mixed $MnO_x/IrO_x$/GC sample (lower panels). Note the difference in scale in the lower left-hand panel, illustrating the relatively low intensity of the Ir 4f signal.*

To probe the electronic structure and the extent of interaction between the two oxides, we performed *ex situ* XPS on a representative $MnO_x/IrO_x$/GC film, as well as on single oxide reference samples termed $MnO_x$/GC and $IrO_x$/GC. Core-level Ir 4f scans were performed, as this peak is considered a reliable probe for determining the average Ir oxidation state.[250,270,271] The magnitude of the Mn 3s peak multiplet splitting serves a similar function in Mn.[272,273] Additional narrow spectra of the O 1s and Cl 2p peaks are shown in the supporting information (Figure A 9.6.20 and Figure A 9.6.21). In Figure 6.10, the $IrO_x$/GC sample has a $4f_{7/2}$ core-level binding energy of 62.4 eV, with a pronounced asymmetry indicating contributions of multiple oxidation states. The obtained binding energy is close to values reported for hydrous iridium oxides lacking long-range order.[270,274] $IrO_x$/GC has mainly $Ir^{4+}$ centers but a significant contribution of $Ir^{3+}$ is apparent, with an estimated $Ir^{3+}$: $Ir^{4+}$ ratio of 0.27. The $MnO_x$/GC sample shows a Mn 3s peak splitting of 5.1 eV, corresponding to an average oxidation state in-between 3+ and 4+. The non-integral average oxidation states of $IrO_x$ and $MnO_x$ suggest non-stoichiometric oxides and disordered structures, consistent with the diffraction experiments. In the $MnO_x/IrO_x$/GC sample, Mn peaks dominate the spectral features (Figure A 9.6.19). Most of the signal originates from the $MnO_x$ overlayer, as was also verified from appearance of a large O 1s contribution at 529.9 eV, and by comparing Mn:Ir ratios determined from XPS and amperometry deposition data (Table A 9.6.2). It was nonetheless still possible to observe the Ir 4f peak, with a peak fitting-derived binding energy of approximately 62.5 eV (see Figure 6.10), a shift of +0.1 eV relative to $IrO_x$/GC. The signal intensity was too weak for a more elaborate peak deconvolution. A relevant question is whether the Ir sites contributing to the weak Ir 4f peak are covered by $MnO_x$, which was suggested by the SEM measurements. The reductive charge $Q_{MnO_x}$ of grown $MnO_x$ films corresponds to a layer roughly 10 nm thick, approaching the limit for the detection depth of XPS. The weak Ir 4f peak in the sample shows strong prevalence of inelastic scattering in the form of tailing at higher binding energies, and a rise in background scattering that is disproportionately higher than the $IrO_x$/GC reference

(Figure A 9.6.22). It can therefore be assumed that the weak XPS Ir 4f peaks originate from sub-surface Ir, and that this Ir must be in intimate contact with the MnO$_x$ layer. The Mn 3s peak splitting in MnO$_x$/IrO$_x$/GC is 5.2 eV, a difference of +0.1 eV with respect to the MnO$_x$/GC reference sample. This shift may indicate a lowering of the average oxidation state,[272] but the shift is small and negligible within the margins of experimental error (± 0.1 eV).

Summarizing our structural studies, we find that the formed MnO$_x$ and IrO$_x$ are amorphous and probably form non-stoichiometric oxides. The MnO$_x$ catalyst without IrO$_x$ showed no activity in OLEMS, and we could also see no evidence of a strong interaction between Mn and Ir from the almost identical Ir 4f binding energies and Mn 3s multiplet splitting in XPS. This makes it doubtful whether the proximity of and interaction with IrO$_x$ could somehow activate MnO$_x$ for the OER.

### *6.3.3. Isotopically labelled OLEMS measurements and OER studies on an RDE*

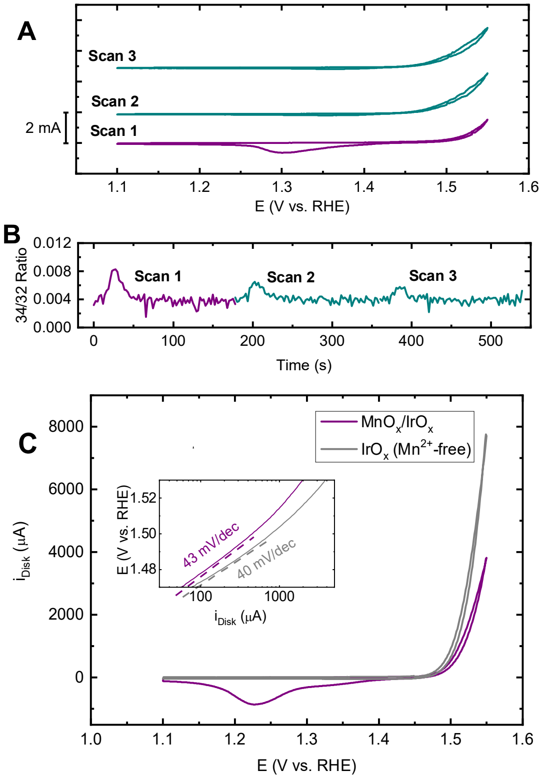

*Figure 6.11: A and B: OLEMS measurements of an 'MnO$_x$/Ir$^{18}$O$_x$/GC' electrode in 0.5 M KHSO$_4$, 30 mM KCl, and 1.2 mM MnSO$_4$ (pH = 0.87). The isotopic labelling procedure is described in the text. The electrode was scanned three times (A), while monitoring the mass/charge ratio 34/32 (B). Scan rate: 5 mV s$^{-1}$. C: CVs of an IrO$_x$/GC rotating disk electrode in 0.5 M Na/HClO$_4$ (pH = 0.85), in a Mn$^{2+}$-free solution (grey) and in presence of 0.6 mM Mn(ClO$_4$)$_2$ with a preconditioned MnO$_x$ film before initiating the forward scan at 1.45 V (purple). Inset shows calculated Tafel slopes determined from forward-backward averaged disk currents. Scan rate: 10 mV s$^{-1}$, rotation rate 1500 RPM. All solutions saturated with Ar.*

Given the lack of electronic interaction between $MnO_x$ and $IrO_x$ suggested by the detailed characterization described in the previous section, isotopically labelled OLEMS measurements were undertaken to further probe the origin of the OER/CER selectivity of the $MnO_x/IrO_x$/GC electrode. We also looked more closely into the OER behavior of the selective catalyst using RDE experiments.

In Figure 6.11A and B, we performed isotopic labelling experiments on $MnO_x/IrO_x$/GC in an attempt to determine the origin of the oxygen produced by the catalyst. This is made possible by the tendency of oxygen of the $IrO_x$ lattice to participate in the OER mechanism.[100] First, the $IrO_x$ lattice oxygen was partially exchanged with the $^{18}O$ isotope by performing OER in a 0.1 M $KHSO_4$ solution of 'marked water' ($H_2{}^{18}O$).[99,100] $MnO_x$ was then grown in 'regular water' at 1.45 V (a potential just before the OER onset), and OLEMS measurements were performed on this $Mn^{16}O_x/Ir^{18}O_x$/GC electrode. By observing changes in the ratio of mass/charge signals 34 and 32,[106] we were able to determine whether the oxygen formed originated from $MnO_x$ (leading to $^{16}O_2$ and no enrichment in the m/z 34 signal), or $Ir^{18}O_x$ (partially producing $^{18}O$-$^{16}O$ and changing the 34/32 ratio). At this point, $^{18}O_2$ can also be formed. Unfortunately, the mass charge ratio of this species (m/z 36) coincides with that of $HCl^+$, a species formed in the ionization chamber, and as such this signal is ambiguous. As can be seen in Figure 6.11B, the catalyst shows an enrichment of $^{18}O$ during OER in the first scan. The produced oxygen thus at least partially originates from the subsurface $IrO_x$ layer. The OLEMS experiments were conducted in presence of chloride, which allowed the monitoring and comparison of $MnO_x$ film growth, as well as ensuring that the experimental conditions were as close as possible to previous OLEMS experiments. In scans 2 and 3, a current increase can be seen which is attributable to increased chlorine evolution after $MnO_x$ reductive dissolution, in agreement with results from Figure 6.7. Figure 6.11C shows OER measurements in a $Cl^-$-free solution of an $IrO_x$/GC catalyst with a pre-grown $MnO_x$ film, compared to the same catalyst in a $Mn^{2+}$-free solution. A non-adsorbing $ClO_4^-$ solution was chosen over $HSO_4^-$ in this experiment since it led to higher OER rates and faster $MnO_x$ growth. The two curves arguably have almost identical onset potentials and very similar Tafel slopes (40 vs. 43 mV/dec for $IrO_x$ and $MnO_x/IrO_x$, respectively). Both experiments shown in Figure 6.11 give strong evidence for the conclusion that the $MnO_x$ film itself is inactive for OER, and the OER activity stems from the $IrO_x$ underneath the $MnO_x$ film.

### 6.3.4. General discussion on the origin of the OER/CER selectivity

From the above results, we conclude that a $MnO_x$ film facilitates the selective formation of $O_2$ over $Cl_2$, in agreement with previous literature.[25,31] However, contrary to what was previously assumed (at least implicitly), the results show that $MnO_x$ is not actually a catalytically active phase. This conclusion is in fact in agreement with previous literature as $MnO_x$ is generally not very active for OER in strongly acidic media (pH < 1), and certainly cannot be expected to show significant activity within the potential window employed in this work.[235,240,245,275,276] From the OLEMS results, it is clear that $MnO_x$/GC in absence of $IrO_x$ is not active for either CER or OER in pH ~ 0.9, even at high potentials of 1.8 V (Figure A 9.6.11). Combined with the XPS measurements that indicate very little electronic interaction between $MnO_x$ and $IrO_x$, it is therefore highly unlikely that $MnO_x$ 'takes over' OER and CER catalysis from $IrO_x$ when it is deposited. Another feature that strongly disfavors $MnO_x$ being the active catalyst is the OER ability seen in Figure 6.11C. The $MnO_x/IrO_x/GC$ electrode displayed an OER current of nearly 5 mA * cm$^{-2}$ (electrode area 0.196 cm$^2$) at an overpotential of 300 mV, which is at least three orders of magnitude higher than even the most optimal performing $MnO_x$ catalysts in alkaline media.[258] The OER current also has a Tafel slope of ~43 mV/dec, which is very close to 40 mV/dec, the OER Tafel slope of the unmodified $IrO_x$ catalyst. We note that a Tafel slope of less than 60 mV/dec has never been reported for OER on $MnO_x$ in any pH. Finally, OLEMS experiments with isotopically labeled $IrO_x$ (Figure 6.11A and B, first scan) show that the $IrO_x$ partakes in OER, despite the existence of a $MnO_x$ layer.

Instead of $MnO_x$ being an exceptional catalyst that breaks the apparent scaling between the CER and OER, we suggest that the catalytically inert $MnO_x$ functions as a porous overlayer that disfavors the transport of chloride ions, as was previously proposed by Bennet.[25] Previous literature suggests that $MnO_x$ deposited at a constant anodic potential usually forms $\gamma$-$MnO_2$ (Nsutite) or $\delta$-$MnO_2$ (Birnessite) motifs, where formation of $\delta$-$MnO_2$ seems preferred over $\gamma$-$MnO_2$ in case the $Mn^{2+}$ concentration is in the mM range.[164,265,266,277–279] The $\delta$ and $\gamma$ polymorphs are both nanoporous and readily intercalate water and cations. From Cl 2p XPS measurements (Figure A 9.6.21), we detected the presence of an alkali-metal chloride in the $IrO_x/GC$ electrode, which can be ascribed to NaCl trapped within the mesoporous $IrO_x$ clusters. By contrast, $MnO_x/GC$ displayed no Cl 2p features (despite being grown in a $Cl^-$-containing solution), and neither did $MnO_x/IrO_x/GC$, which we interpret as chloride being unable to penetrate the $MnO_x$ film. Furthermore, in the OLEMS results in Figure 6.7, the $O_2$ signal of scan 1 shows strong tailing, persisting for nearly 100 s after starting the experiment, which translates to $O_2$ detected down to 1.15 V in the backward scan. This effect is ascribed to $O_2$ trapped in the $MnO_x$ porous structure, which is liberated upon $MnO_x$ dissolution.

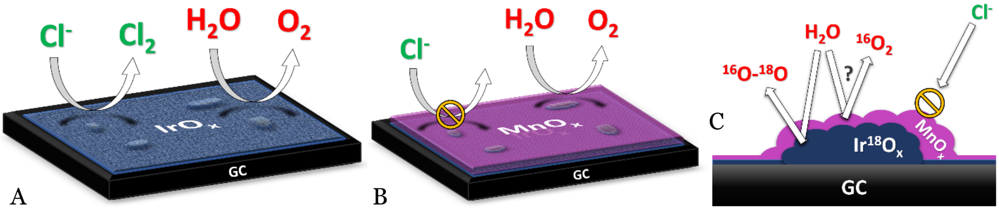

*Scheme 6.1:Sketch of the $IrO_x/GC$ catalyst (A) and the deposition structure of $MnO_x$ deposition on $MnO_x/IrO_x/GC$ (B). The $MnO_x$ forms a porous, amorphous network on top of the $IrO_x$ layer, blocking CER by preventing $Cl^-$ from reaching the $IrO_x$ underneath. A side-view (C) shows the isotopic labelling experiment in Figure 6.11A and B. Participation of sub-surface $IrO_x$ in OER is apparent from detection of the enriched m/z 34 signal.*

Scheme 6.1 illustrates the origin of the observed selectivity behavior with $MnO_x$ deposition. Starting from the 'bare' $IrO_x$ film, initial $MnO_x$ deposition ($0 < Q_{MnO_x} < 2$ mC) is accompanied by a mild and approximately proportional decrease in OER and CER activity (Figure 6.3 and Figure 6.4), implicating that at these low coverages, both reactions are hindered. The corresponding Tafel plots extracted from the rings currents (Figure 6.5 and Figure A 9.6.7) show that the CER slopes retain a value of ~40 mV/dec, but are shifted gradually upwards to higher potentials. A similar effect during the study of CER was reported before by Mozota and

Conway,[280] and would imply a decrease in the number of active sites with an unchanging reaction mechanism. From electron microscopy micrographs, the $MnO_x$ forms a porous network of amorphous sheets. The dramatic selectivity shift at $Q_{MnO_x} > 2$ mC then presumably arises when the growing $MnO_x$ sheets start to intertwine and fully cover the $IrO_x$ electrode. $MnO_x$ deposition at this stage seems to solely inhibit CER, whereas OER remains relatively unaffected, suggesting that at this point, the film growth is intrinsically different from its initial deposition stage. When 'fully grown', the amorphous $MnO_x$ film still seems to allow transport of $H_2O$, $H^+$ and $O_2$ between $IrO_x$ and the electrolyte. The decreased selectivity versus CER can thus be explained on the basis of concentration overpotentials, in line with recent reports on electrocatalysis at 'buried interfaces' by Takanabe et. al.[281] and Esposito *et al.* [282,283] The slow transport of chloride through the $MnO_x$ phase means that near the buried $IrO_x$ interface, both the chloride diffusion coefficient and concentration gradient are lowered. This leads to a significant increase of the diffusion layer thickness and an effective increase in the CER overpotential. We further verified the anion-deflecting behavior of $MnO_x$ by performing OER using a $MnO_x/IrO_x/GC$ catalyst in presence of bromide ions (Figure A 9.6.12). The Pt ring was fixed at $E_R = 0.90$ V, to serve as a probe for bromine reduction. We found that the blocking of bromine evolution is strongly coupled to the presence of the $MnO_x$ film. Lastly, the effect of $MnO_x$ deposition on CER selectivity was verified using a Pt disk electrode as CER catalyst (Figure A 9.6.13). A $MnO_x/Pt$ electrode evolved insignificant amounts of $Cl_2$, whereas the OER onset could be seen near 1.7 V, which is reminiscent of the previously reported OER onset on bare Pt.[284]

$IrO_x$ was also present in the $MnO_x$-based seawater anodes by Hashimoto *et al.*, for which thick heterometal-doped $MnO_x$ coatings were grown on Ti-supported $IrO_x$ ($IrO_x$/Ti). The $IrO_x$ was added with the intention of preventing the formation of insulating $TiO_2$ during electrode operation. We believe the OER selective $Mn_yM_{(1-y)}O_x/IrO_x/Ti$ anodes operate in a similar fashion as our $MnO_x/IrO_x/GC$ catalyst under study, and that the $IrO_x$ layer may have been crucial for the relatively low polarization resistance during the galvanostatic experiments. The OER selectivity effect of different dopants may have been due to modified $MnO_x$ film stability or morphology under the strongly oxidizing operating conditions.

Application of selective blockage of chloride in seawater electrolysis was recently demonstrated by Ravichandran *et al.*[165] An analogous case of selectivity induced by a catalytically inert film is likely at hand in the industrial chlorate process, where $Cr(OH)_3$-coated cathodes are used for selective hydrogen evolution.[34,141,285] The $H_2$-selectivity of the chromium film has been suggested to stem from the selective blocking of dissolved $ClO^-$ anions and oxygen. Interestingly, $MnO_x$ has been recently suggested as a promising alternative to the use of Cr(VI) for the selective hydrogen evolution.[286]

## 6.4. Conclusion

In this chapter, we have investigated the unusual OER over CER selectivity of $MnO_x$ based anodes in the context of hydrogen production from acidic saline water electrolysis. Deposition of a thin $MnO_x$ film onto glassy carbon-supported $IrO_x$ moderately decreases the catalytic activity and strongly shifts the product selectivity from $Cl_2$ towards $O_2$, once a critical $MnO_x$

film charge $Q_{MnO_x}$ of approximately 2 mC (10 mC cm$^{-2}$) is reached. The $\mathrm{MnO_x}$ deposit is catalytically inactive, and instead seems to function as a diffusion barrier that prevents $\mathrm{Cl^-}$ from reacting on the $\mathrm{IrO_x}$ catalyst underneath, while still facilitating the transport of water, protons and $\mathrm{O_2}$ between $\mathrm{IrO_x}$ and the electrolyte, necessary for OER activity. The results of this work fit in an emerging trend of using diffusion barriers to affect selectivity. This may be a promising approach in practical brine electrolysis, in contrast to finding an OER catalyst that breaks the intrinsic scaling between selectivity and activity.